

Chapter 4

Polarisation–Tilt Coupling and Thermal Variation of Pitch in the Chiral Smectic C Phase

4.1 Introduction

Since the discovery of ferroelectricity[1] in liquid crystals, this area of research has been very active both from the point of view of basic physics and technological applications. As discussed in earlier chapters, the smectic C (C) phase exhibits ferroelectric properties[1,2] if the constituent molecules are optically active. An important structural feature of this chiral smectic C (C*) phase is that the azimuthal direction of the tilt of the molecules precesses from one layer to another giving rise to a helix. The pitch of the helix is given by $\frac{2\pi}{q}$, where q is the wave vector of the helix. Due to the chirality of the molecules, the tilt ordering breaks the mirror symmetry within the layers and induces a transverse in-plane polarisation perpendicular to the tilt. Thus the C* phase exhibits a spontaneous polarisation P_S .

Although considerable experimental and theoretical work has been done in characterising the bulk properties of ferroelectric C* phase, the nature of the coupling between the magnitude of tilt θ and polarisation P_S has not been well understood. A simple theoretical approach[3] expects

1. the spontaneous polarisation (P_S) and tilt angle(θ) to be coupled in a linear way, i.e., the ratio $\frac{P_S}{\theta}$ is independent of temperature.
2. The helical pitch $p (= \frac{2\pi}{q})$ to be invariant with respect to temperature.

However, experimental observations are not in accord with these predictions. In particular, the ratio $\frac{P_S}{\theta}$ is weakly dependent on temperature deep in the C* phase, but shows a strong variation near the transition to the A phase[4,5,6].

Likewise, far below the transition, the pitch increases slowly with temperature and shows a maximum below the transition temperature T_{AC^*} [4,7,8]. Based on these experimental observations carried out mainly on p-decyloxy benzyli-dene p-amino - 2 - methylbutyl - cinnamate (DOBAMBC), extended mean field models[9,10,6], with as many as eleven expansion coefficients were proposed. In these models, in addition to the terms considered in the simple model, a sixth order term in tilt[11,12] and a biquadratic polarisation-tilt coupling term[9,10] are also taken into account.

Most of the measurements that exist in the literature[4,13,14] present results wherein not enough attention has been given to the region close to T_{AC^*} . The few high resolution studies[6,15] have been done on materials exhibiting a low value of spontaneous polarisation. In other words, systematic studies on substances exhibiting different degrees of polarisation to tilt coupling have not been performed. With this in view, we have undertaken a detailed study of temperature variation of polarisation, tilt angle and pitch in three different materials having varying degree of P_S value. The results obtained are compared with the predictions of the extended mean-field model[10] as well as that of a recent microscopic model[16,17] based on a single particle potential.

We begin the discussion with an outline of the symmetry arguments giving rise to the ferroelectricity in the C^* phase and a description of a simple phenomenological model and its inadequacy in explaining the experimental results. Next, we give a brief summary of the extended mean-field model and the microscopic model. This is followed by a description of the techniques employed to

measure the thermal variation of P_S , θ and pitch p . Later the results obtained for the three different materials are discussed. Finally, the experimental data are compared with the predictions of the theoretical models,

4.1.1 Symmetry arguments

The smectic C phase has a monoclinic symmetry containing three symmetry elements, viz., a two-fold rotation axis (C_2) normal to the tilt direction, a mirror plane, m , normal to the two-fold axis and a centre of inversion, i , as shown Figure 4.1. If the molecules are chiral, the mirror plane and the centre of inversion vanish. Assuming that the system has a polarisation vector \vec{P}_S it can be checked whether this vector is invariant under all symmetry operations permitted in the phase under consideration. In both C and C* phases, a 180° rotation around the two-fold axis (C_2 axis) is an allowed symmetry operation. Under this operation, the polarisation vector \vec{P}_S transforms according to $(P_x, P_y, P_z) \rightarrow (-P_x, P_y, -P_z)$. In the absence of chirality (C phase), a reflection from the mirror plane (m) in the C phase, transforms \vec{P}_S according to $(0, P_y, 0) \rightarrow (0, -P_y, 0)$ leading to $P_y=0$. Thus the C phase cannot have a polarisation. In the case of C* phase, since there is no mirror plane, the system exhibits a non-zero spontaneous polarisation along the two-fold axis. Thus the C* phase is ferroelectric. However, the presence of helix, i.e., the precession of the azimuthal direction of tilt of the molecules from one layer to another, averages out the spontaneous polarisation to zero. To obtain a non-zero macroscopic polarisation the helix has to be unwound by an external field, such as electric field[2], or shear[18] or by surface interactions[19].

Chapter 4: Polarisation-Tilt Coupling and thermal variation of **Pitch**..

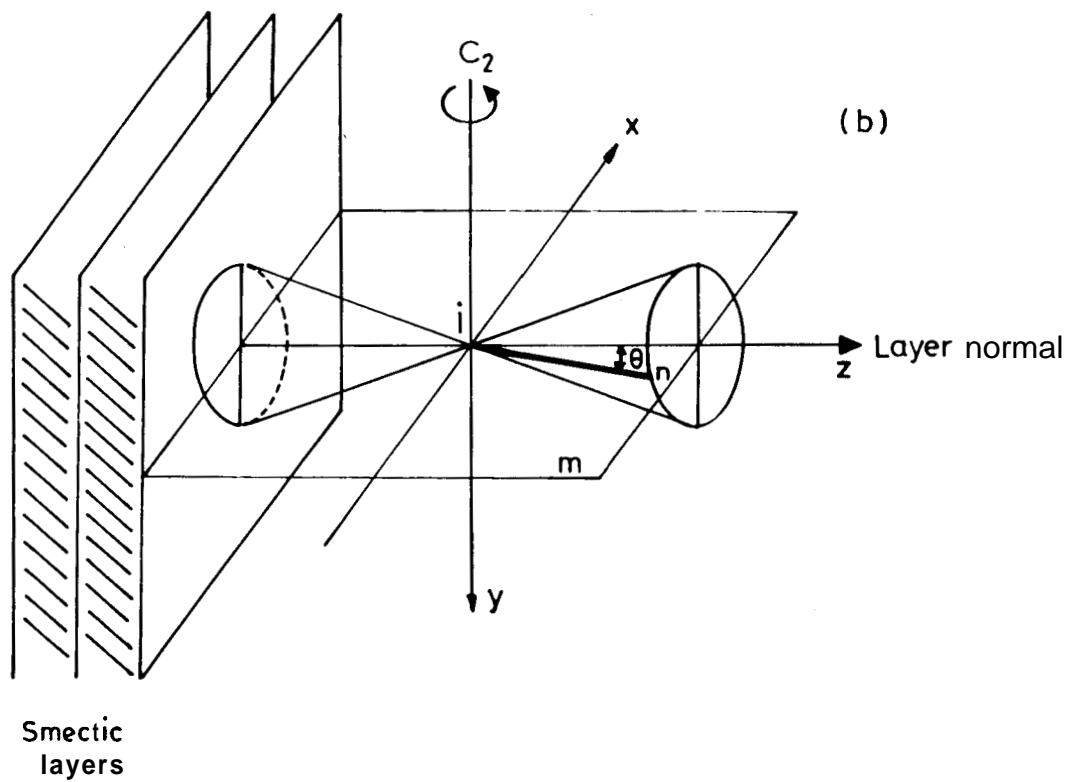


Figure 4.1: Symmetry elements of the C phase, m - the mirror symmetry, i - center of inversion, C_2 - two fold axis. In the C^* phase only C_2 remains.

4.1.2 Phenomenological models

At a phenomenological level, a transition between two phases can be explained by considering the free energy of the system written in terms of an order parameter keeping in view the symmetry properties of the medium. Thus for the present case the obvious choice of the order parameter would be the spontaneous polarisation P_S . But, as we have already mentioned in Chapter 2, contrary to the situation in a majority of solid ferroelectrics, experimental evidences show that in the ferroelectric smectics, P_S does not drive the paraelectric –ferroelectric transition. In fact, Meyer realised that the transition is brought about by the tilting of the molecules and polarisation becomes finite only as a consequence of it[2]. Hence the natural choice for the primary order parameter is the tilt. Keeping this in view, he proposed[2] a free energy expression in which θ and P_S were coupled in a linear way. This model was further developed by Pikin and Indenbom[3] which we will describe here briefly. For the sake of convenience let us refer to this model as P-I model. The free energy of the system is expanded in terms of the primary two component tilt order parameter $\vec{\xi} = (\xi_1, \xi_2)$ which is the projection of the director \hat{n} onto smectic planes and the secondary order parameter, the \vec{P}_S , which is always at right angle to $\vec{\xi}$ [1]. The helix is chosen to be along the Z axis. The coordinates used are shown in Figure 4.2. Thus the order parameters are $\vec{\xi} = \xi_1 \hat{x} + \xi_2 \hat{y}$ and $\vec{P}_S = P_x \hat{x} + P_y \hat{y}$.

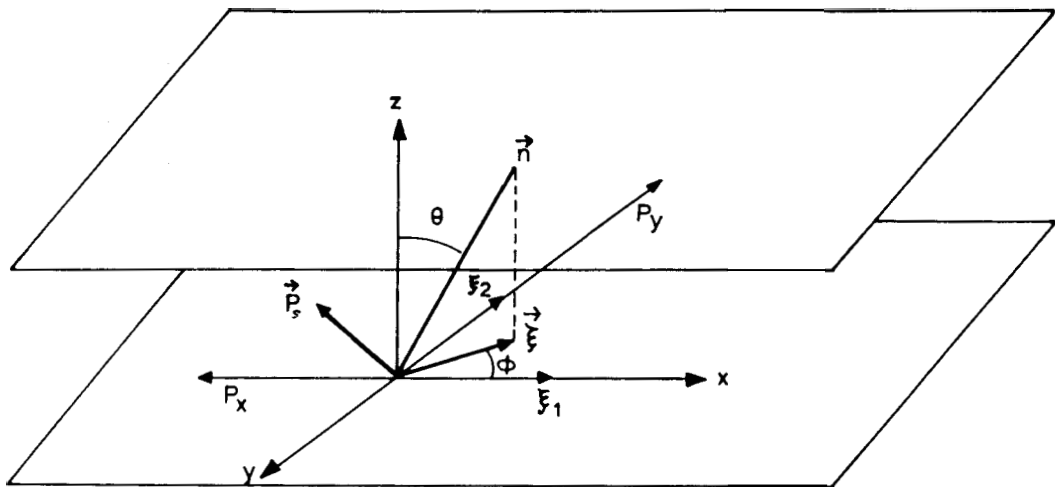


Figure 4.2: Definition of coordinate system and the order parameters

The free energy density is written as,

$$\begin{aligned}
 g(z) = & \frac{1}{2}a(\xi_1^2 + \xi_2^2) + \frac{1}{4}b(\xi_1^2 + \xi_2^2)^2 - \Lambda \left(\xi_1 \frac{d\xi_2}{dz} - \xi_2 \frac{d\xi_1}{dz} \right) \\
 & + \frac{1}{2}K_3 \left[\left(\frac{d\xi_1}{dz} \right)^2 + \left(\frac{d\xi_2}{dz} \right)^2 \right] + \frac{1}{2\epsilon} (P_x^2 + P_y^2) \\
 & - \mu \left(P_x \frac{d\xi_1}{dz} + P_y \frac{d\xi_2}{dz} \right) + C(P_x \xi_2 - P_y \xi_1) \quad (4.1)
 \end{aligned}$$

where $a = \alpha(T - T_o)$, T being the temperature of the system. T_o is the phase transition temperature of the corresponding racemic mixture. $b > 0$ for a second order A-C* transition. K_3 is the elastic modulus, Λ the coefficient of the Lifshitz term responsible for the twist-bead modulation, μ and C are the coefficients of ' flexo- ' and ' piezo- ' electric coupling between θ and P_S .

For small tilt angles,

$$\xi_1 \simeq \theta \cos \phi$$

$$\xi_2 \simeq \theta \sin \phi$$

where ϕ is the azimuthal angle determining the orientation of \hat{n} with respect to the smectic layer normal.

In terms of the helical wave vector q , the components of the two order parameters can be written as

$$\xi_1 = \theta \cos qz$$

$$\xi_2 = \theta \sin qz$$

$$P_x = -P_S \sin qz$$

$$P_y = P_S \sin qz \quad (4.2)$$

Substituting in Equation 4.1 we get,

$$g(z) = \frac{1}{2}a\theta^2 + \frac{1}{4}b\theta^4 - \Lambda q\theta^2 + \frac{1}{2}K_3q^2\theta^2 + \frac{1}{2\epsilon}P_S^2 - \mu q P_S\theta - C P_S\theta \quad (4.3)$$

Minimising this equation with respect to P_S , θ and q yields the expressions for transition temperature T_{AC^*} , the temperature dependence of θ , P_S and p as follows:

$$\begin{aligned} T_{AC^*} &= T_o + \frac{1}{\alpha}[\epsilon C^2 + (K_3 - \epsilon\mu^2)q^2] \\ \theta &= \left(\frac{\alpha}{b}\right)^{1/2} (T_{AC^*} - T)^{0.5} \\ P_S &= \epsilon(\mu q + C)\theta \\ p &= \frac{2\pi}{q} = 2\pi \left(\frac{K_3 - \epsilon\mu^2}{\Lambda + \epsilon\mu C} \right) \end{aligned} \quad (4.4)$$

Thus the model predicts,

1. The polarisation P_S is proportional to the tilt angle θ . i.e., $\frac{P_S}{\theta} = \text{constant}$.
2. The helical pitch p is temperature independent.

4.1.3 Experimental facts

Earlier measurements of polarisation (P_S) and tilt angle (θ) seemed to support some of the predictions of the above model. However, the recent quasi simultaneous high resolution measurements[6] of P_S and θ have shown that deep in the C^* phase the ratio $\frac{P_S}{\theta}$ is weakly dependent on temperature but shows a very strong variation near the transition to the A phase. Likewise, far below the

transition, the pitch increases slowly with temperature but shows a pronounced maximum below the transition temperature, T_{AC^*} .

Figure 4.3 shows the qualitative disagreement between the predictions of the P - I model and the experimentally measured thermodynamical properties.

4.1.4 Extended mean-field model

In order to explain the experimental results shown in Figure 4.3(b) (obtained using DOBAMBC) an 'extended mean-field model'(EMF model)[9,10,6] with as many as eleven expansion coefficients was proposed. Here, in addition to the terms considered in the P-I model, a sixth order term in tilt[11,12] and a biquadratic polarisation- tilt coupling term[9,10] are also taken into account. The free energy density is given by,

$$g(z) = \frac{1}{2}a\theta^2 + \frac{1}{4}b\theta^4 + \frac{1}{6}c\theta^6 - \Lambda q\theta^2 + \frac{1}{2}K_3q^2\theta^2 + \frac{1}{2\epsilon}P_S^2 - \mu qP_S\theta - CP_S\theta - \frac{1}{2}\Omega P_S^2\theta^2 + \frac{1}{4}\eta P_S^4 - dq\theta^4 \quad (4.5)$$

The biquadratic coupling term ($\Omega P_S^2 \theta^2$) implies that the tilt induces a transverse quadrupole moment in chiral as well as non-chiral systems. Close to the transition, i.e., when θ is quite small, the $P_S - \theta$ coupling is dominated by the bilinear term ($CP_S\theta$) but away from it the biquadratic term takes over. This change-over has been shown to account for the complex behaviour of $\frac{P_S}{\theta}$ ratio and the pitch. It was also realised that the heat capacity profiles across the A-C/A-C* transition can be satisfactorily explained by including a sixth order ($c\theta^6$) term in the free energy[11,12]. As we have already discussed in Chapter 3 the presence of this sixth order term implies that the transition is close to a mean-field

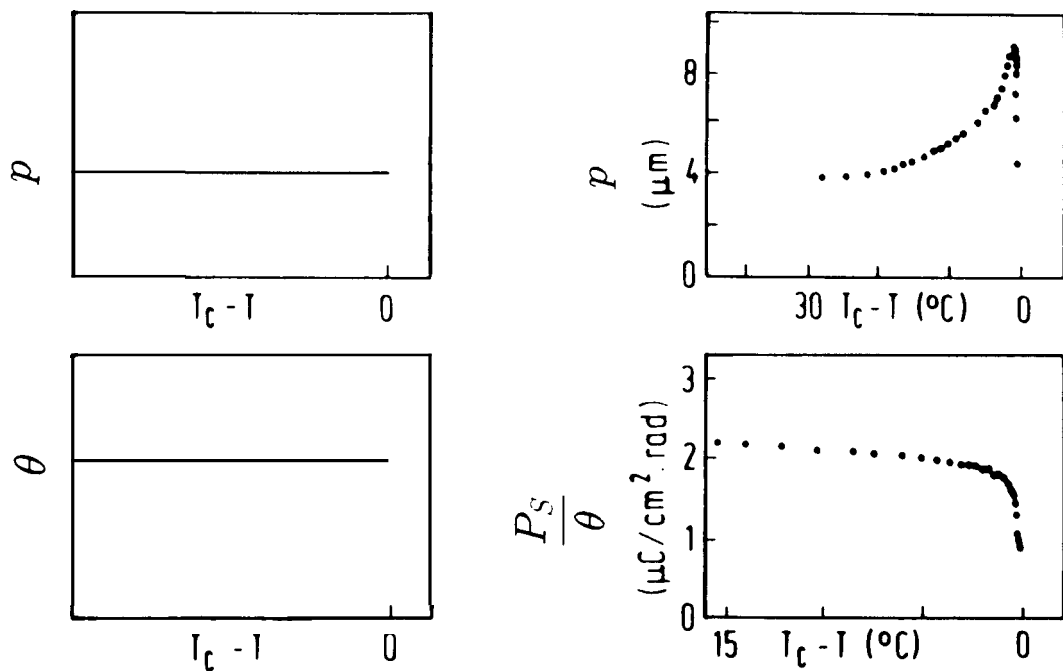


Figure 4.3: (a) Predictions of the P-I model and (b) the experimental observations of pitch (from ref.[4]) and $\frac{P_s}{\theta}$ (from ref.[6])

tricritical point. The last term in Equation 4.5 is used to explain the monotonic increase of the pitch with temperature away from the transition, while the P^4 term is added to stabilize the system.

In order to reduce the number of coefficients, Equation 4.5 is written in a dimensionless form as given below:

$$\tilde{g} = \frac{1}{2}(\beta_c^2 - \gamma\tau)\tilde{\theta}^2 + \frac{1}{4}\gamma\tilde{\theta}^4 + \frac{1}{6}\rho\tilde{\theta}^6 + \frac{1}{2}\tilde{P}^2 - \beta_c\tilde{P}\tilde{\theta} - \frac{1}{2}\tilde{P}^2\tilde{\theta}^2 + \frac{1}{4}\tilde{P}^4 - \nu\delta\tilde{P}\tilde{\theta}^3 \quad (4.6)$$

where $\tilde{P} = \frac{P_S}{P^*}$, $\tilde{\theta} = \frac{\theta}{\theta^*}$, $\tau = \left(\frac{T_{AC^*} - T}{T^*}\right)$. The parameters with asterisk are the normalising quantities.

Minimising \tilde{g} with respect to \tilde{P} ,

$$\tilde{P}^3 + (1 - \tilde{\theta}^2)\tilde{P} - (\beta_c + \nu\delta\tilde{\theta}^2)\tilde{\theta} = 0 \quad (4.7)$$

In the limit $\nu\delta \ll \beta_c$, Equation 4.7 can be written as,

$$\tilde{P}^3 + (1 - \tilde{\theta}^2)\tilde{P} - \beta_c\tilde{\theta} = 0 \quad (4.8)$$

β_c is an all important coefficient in this model and is expected to determine the nature of the thermal variation of $\frac{P_S}{\theta}$ ratio and the helical pitch. Numerically β_c is the ratio of the bilinear to biquadratic coupling terms.

$$\beta_c = \frac{\tilde{\epsilon}\tilde{C}\eta^{1/2}}{\Omega^{1/2}} \quad (4.9)$$

The theoretical curves for $\frac{P_S}{\theta}$ ratio and pitch p are shown in Figure 4.4. It is seen that there is good agreement between the predictions of the EMF model and the experimental features seen in Figure 4.3(b).

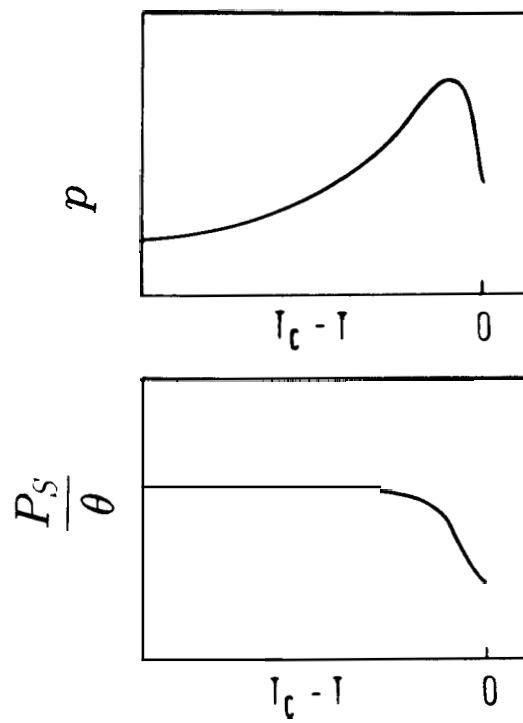


Figure 4.4: Theoretical curves for p and $\frac{P_s}{6}$ as predicted by the extended mean-field model.

4.1.5 Microscopic model

With a view of giving a microscopic explanation for the origin of ferroelectricity, Zeks et al[16], proposed a model based on a single particle potential. The main assumption in this model[16,17] is that the ordering of the transverse electric dipoles (of moment μ) is induced by the hindered rotation of the tilt of the molecules. The orientation of the dipoles in the plane perpendicular to the long molecular axis is defined by an angle ψ . The single particle potential describing such a system is written as

$$U = -a_1\theta\cos\psi - a_2\theta^2\cos 2\psi \quad (4.10)$$

The first term on the right is of chiral character and is analogous to the piezoelectric bilinear coupling in the EMF model. The second term is quadratic in θ and is of non-chiral character and causes a quadrupolar ordering in the direction perpendicular to the tilt (for $a_2 > 0$). This term is analogous to the biquadratic coupling term in the EMF model. The expected relation between the magnitudes of the two parts of the potential is $a_1\theta \ll a_2\theta^2$, because the chiral interactions are supposed to be weak except in the vicinity of T_{AC^*} where θ is very small.

Using this form of the potential, Buka et al[20] have worked out an expression for the temperature dependence of P_S .

$$P_S = \rho\mu \langle \cos \psi \rangle \quad (4.11)$$

where ρ is the number density of the molecules, and

$$\langle \cos \psi \rangle = \frac{\int_0^{2\pi} \cos \psi \exp(-U/kT) d\psi}{\int_0^{2\pi} \exp(-U/kT) d\psi} \quad (4.12)$$

Here k is the Boltzmann constant and T is the absolute temperature. Expanding $\exp(-U/kT)$ in a series, keeping terms up to second order and carrying out the integration we get,

$$P_S = \rho\mu\theta a_1 \frac{2kT + a_2\theta^2}{4(kT)^2 + (a_1\theta)^2 + (a_2\theta^2)^2} \quad (4.13)$$

By neglecting higher order terms in θ , Equation 4.13 can be written as

$$P_S = A_1\theta \left[\frac{A_2T + A_3\theta^2}{T^2 + A_2^2\theta^2} \right] \quad (4.14)$$

where $A_1 = \rho\mu$, $A_2 = a_1/2k$, $A_3 = \frac{a_1a_2}{4k^2}$ Equation 4.14 can be used to evaluate A_1 , A_2 and A_3 from the experimental data and hence the chiral as well as the non-chiral parts of the potential can be determined.

4.2 Experimental

4.2.1 Materials used

Measurements of P_S , θ and p have been carried out on three different compounds whose structural formulae and the transition temperatures are given in Table 4.1. Compound I is p-octyloxy benzylidene p-amino-2-methylbutylcinnamate (OOBAMBC)[21], the 8th homologue of the well known nOBAMBC series. Compound II and compound III are derivatives of *trans-p-n*-alkoxy cinnamate[22].

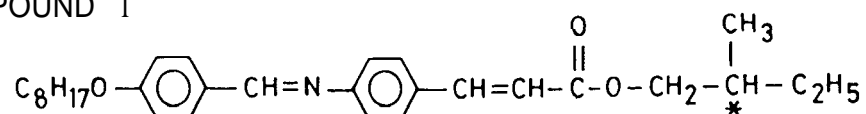
4.2.2 Spontaneous Polarisation measurements

Thermal variation of the spontaneous polarisation P_S was measured using a calibrated Diamant Bridge technique[23]. The Bridge was set up by S. M. Khened

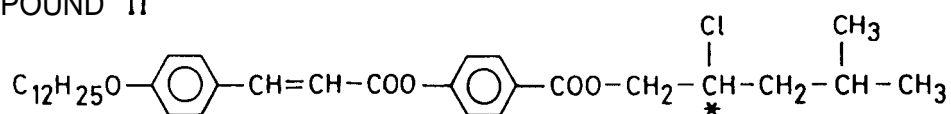
Chapter 4: Polarisation-Tilt Coupling and thermal variation of Pitch...

Table 4.1: Structural formulae and transition temperatures ($^{\circ}\text{C}$) of the materials used.

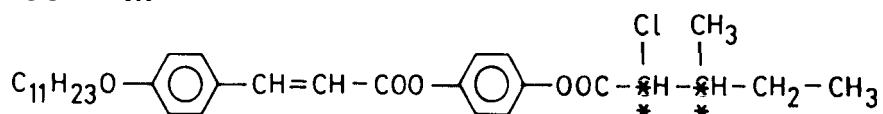
COMPOUND I



COMPOUND II



COMPOUND III



Material	Iso	A	C*	I*
compound I	.	118.7	. 94.2	. 67.0 .
compound II	.	81.0	. 65.5	. -
compound III	.	99.5	. 83.5	. -

Iso= isotropic phase, A = smectic A

C = smectic C, C* = chiral smectic C

I* = chiral smectic I phase.

and is described in greater detail in his thesis[24]. We will mention only the important points here.

The sample cell was made up of two ITO - coated glass plates which had the electrode pattern etched on to them. The glass plates were treated with polyimide solution and rubbed unidirectionally in order to obtain a homogeneously aligned sample. Mylar spacers were used to define the thickness of the cell. Care was taken to see that neither the spacer nor the bonding adhesive was present inside the active area. The actual thickness of the cell (typically $\sim 12 \mu\text{m}$) was measured using an interferometric technique. The active area of the cell A , was calculated by measuring the capacitance C_o of the empty cell as follows: $A = \frac{C_o d_c}{\epsilon_o}$ where d_c is the thickness of the cell and ϵ_o is the permittivity of the free space. The sample was filled into the cell in the isotropic phase by capillary action. It was later kept inside a temperature controlled oven. The sample was heated to a temperature slightly above the isotropic point and cooled slowly ($2\text{-}3^\circ \text{C}/\text{hour}$) across the isotropic-smectic A (Iso-A) transition. This procedure usually resulted in a monodomain A phase. In some cases application of a magnetic field [an electromagnet (Bruker B-E 25) giving 2.4 T field] was used. In order to retain the alignment the sample was cooled slowly from the A phase to C* phase. The spontaneous polarisation was measured in the following manner.

The Diamant Bridge set up is shown schematically in Figure 4.5. One arm of the bridge contains the sample cell and the other a resistor - capacitor combination C_B and R_B (both of which can be varied independently). $C_B - R_B$ combination was used to balance the bridge by compensating for ionic and linear

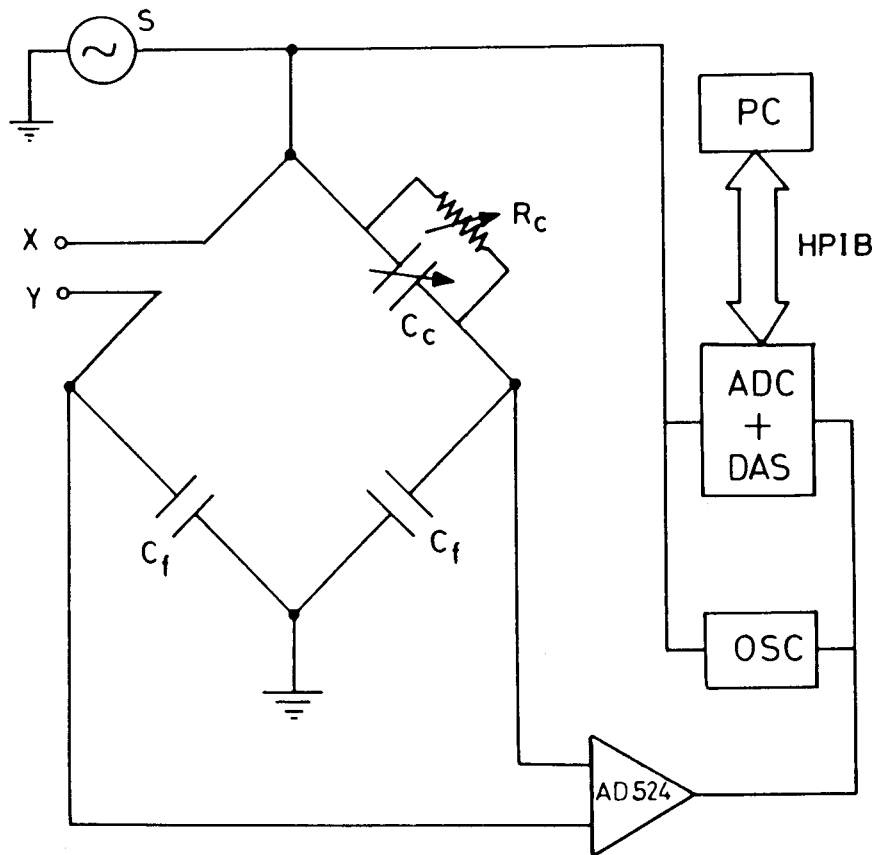


Figure 4.5: Diamant Bridge set up.

- S—signal source,
- X, Y—sample leads,
- R_c , C_c —compensating resistor, capacitor combination,
- C_f —fixed capacitor,
- OSC—dual channel storage oscilloscope,
- ADC+DAS—Analog-Digital converter and data acquisition system,
- PC—personal computer,
- AD524—programmable gain operational amplifier.

capacitive portions of output signal. Two fixed value capacitors ($C_f = 0.1 \mu\text{ F}$) form the other two arms of the bridge. A function generator (HP 8116) in conjunction with a high voltage high fidelity amplifier (Kepco BOP 1000 M) was used to apply a sine wave voltage to the sample. The output from the 'sample arm' and the 'compensating arm' of the bridge were fed to a programmable - gain difference amplifier (Analog Devices AD524) to produce a hysteresis loop. The applied and the amplified output signals were digitised using a digitiser - cum - data acquisition system (HP 7090. A). The data thus collected was transferred to an online computer (HP 86B) for storage. The temperature was measured using a low drift nanovoltmeter (Keithley 181). By measuring the amplitude V_p of the output wave, P_S was calculated using the relation,

$$P_S = \frac{C_f V_p}{A_c} \quad (4.15)$$

where C_f is the value of the standard capacitor and A_c , the active area of the sample cell. The relative accuracy in the determination of P_S was $\sim \pm 0.1 \text{ nC/cm}^2$.

4.2.3 Tilt angle measurements

Tilt angle θ was measured using the X-ray diffraction set up described in Chapter 2.

4.2.4 Pitch measurements

A standard optical diffraction method[25,26] was employed to measure the helical pitch p . The sample was sandwiched between two ITO coated glass plates. Mylar spacers were used to define the sample thickness ($\sim 125 \mu\text{m}$). The cell was kept

inside a temperature controlled oven. A homogeneously aligned (book shelf geometry) was obtained by cooling the sample from isotropic to A phase in the presence of a magnetic field (2.4 T) at a rate 3° C/hour. The homogeneously aligned C* phase acts as a optical phase grating. A He-Ne laser beam ($\lambda = 0.6328 \text{ cm}$) was passed through the sample perpendicular to the helical axis. The diffraction pattern which was made to fall on a screen consisted of first order and sometimes higher order spots. Figure 4.6 shows a typical diffraction pattern obtained. The pitch p was calculated using the equation,

$$p = \frac{\lambda}{\sin \Theta'} \quad (4.16)$$

where $\Theta' = \tan^{-1} \left(\frac{r}{D} \right)$ where r is the distance between the main beam and the diffracted beam at the image plane and D is the distance between the sample and the screen.

For acquiring and analysing the diffraction pattern we have adopted a novel method, using which we were able to measure r with a high precision. The diffraction pattern on the screen was captured by a high resolution video camera (Philips VK 4033) and was recorded on a video tape for storage and analysis. This enabled collection of data at close intervals of temperature. The off-line analysis part consisted of a high resolution - 262 K pixels / Frame and 8 bit data resolution, Frame Grabber card with 0.5 MB on-board memory in conjunction with a Frame processor board (Data Translation DT 2851 and DT 2858) both of which were plugged into PC AT I/O slots. The cards accept the standard RS-170 PAL input and can be accessed and controlled through a high-level-language interface software. A user-written Fortran program converted the 'image' files

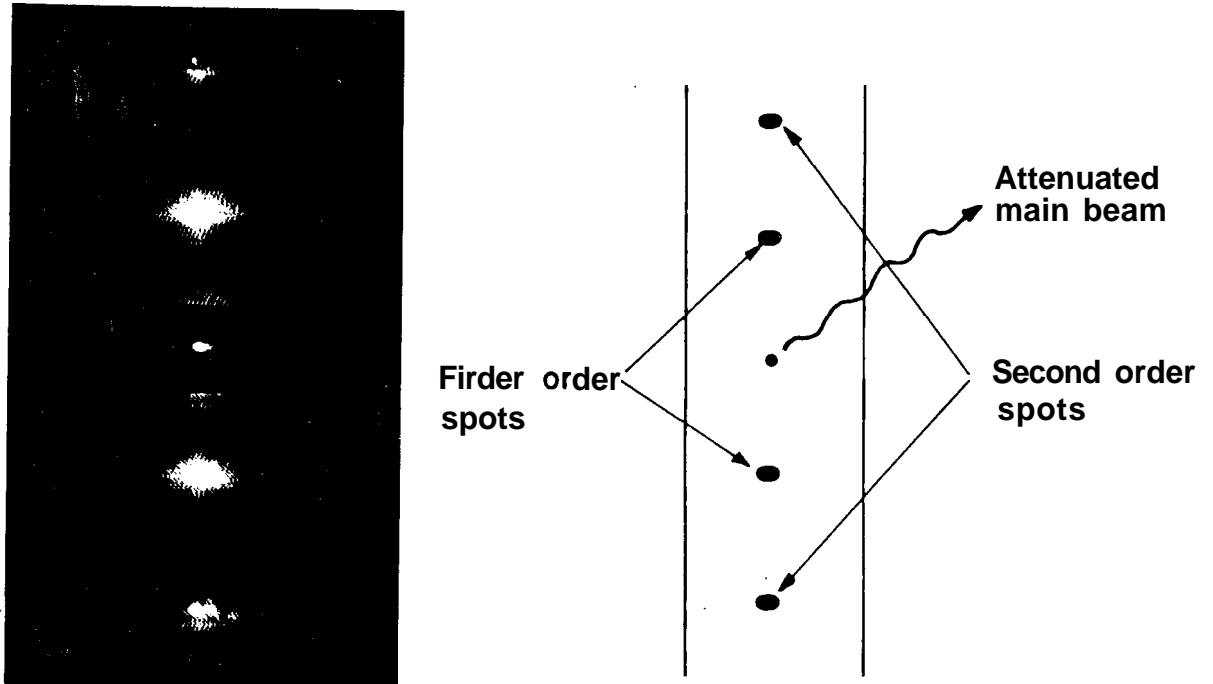


Figure 4.6: Typical optical diffraction spots. The schematic of the pattern is shown on the right.

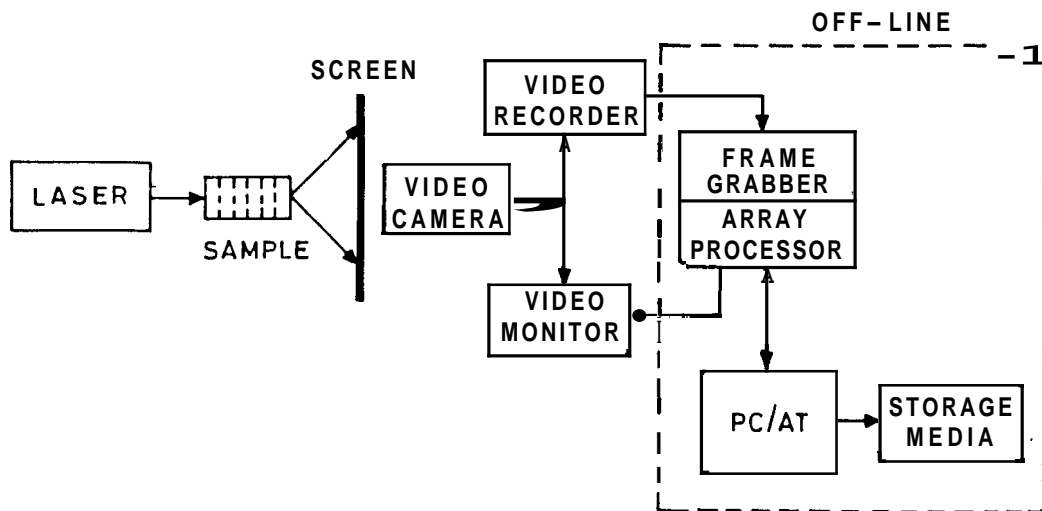


Figure 4.7: Block diagram of the set up used for pitch measurements.

into ASCII format files which were later analysed using a peak finding macro program written in a commercial software environment (Quattro-Borland). The schematic diagram of the set up is given in Figure 4.7. The calibration of this set up was checked by measuring the pitch as a function of temperature for 4-(2'-methylbutyl) phenyl 4'-n-octyl biphenyl-4-carboxylate (CE8)[27]. The plot of temperature variation of pitch for CE8 is shown in Figure 4.8. Our data agreed to within 2% of the value reported earlier[28] using a sophisticated light scattering technique.

4.3 Results and Discussion

Figures 4.9, 4.10 and 4.11 show the temperature variation of spontaneous polarisation (P_S) and tilt angle (θ) in the C* phase for compound I, compound II and compound III respectively. It is clear that the P_S value for compound III is highest ($\sim 80\text{nC/cm}^2$ at $T_{AC^*} - T = 7\text{K}$) among the three materials and is lowest for compound I ($\sim 2\text{nC/cm}^2$ at $T_{AC^*} - T = 7\text{K}$). Both P_S and θ vary continuously as a function of temperature and go to zero at the transition, showing that the A-C* transition is second order in these materials. Although a simple power law of the type

$$\theta = \theta_0 t^{\beta_1} \quad (4.17)$$

and

$$P_S = P_0 t^{\beta_2} \quad (4.18)$$

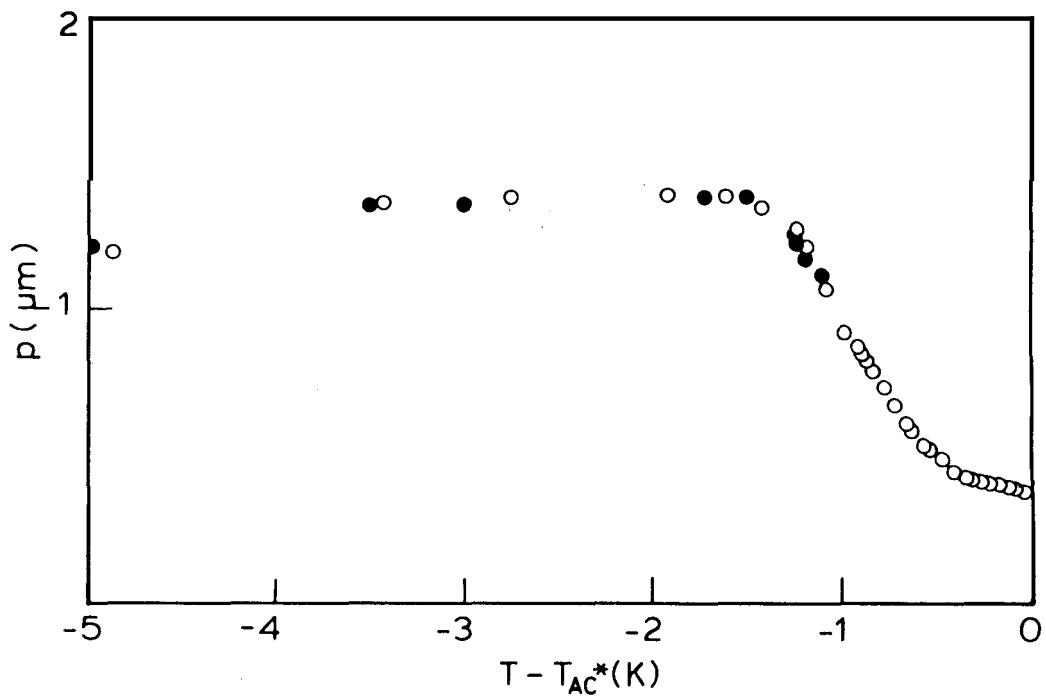


Figure 4.8: Temperature variation of pitch for CE8. Closed circles represent data obtained using our set up and open circles data adopted from ref.[27].

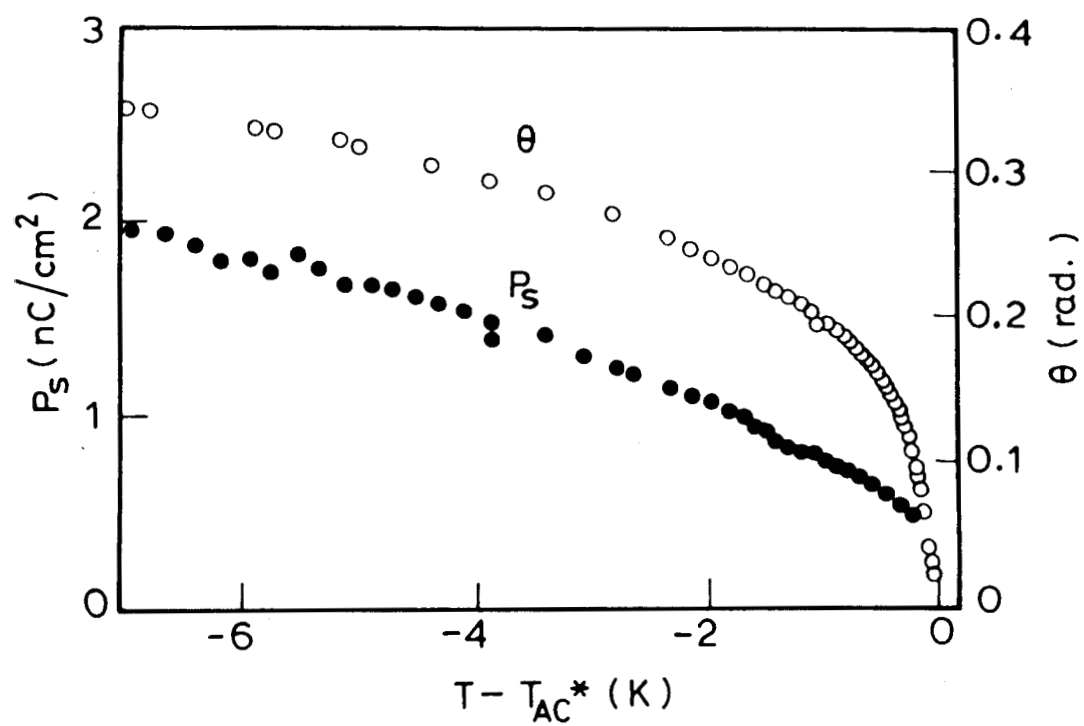


Figure 4.9: Thermal variation of P_S and θ for compound I.

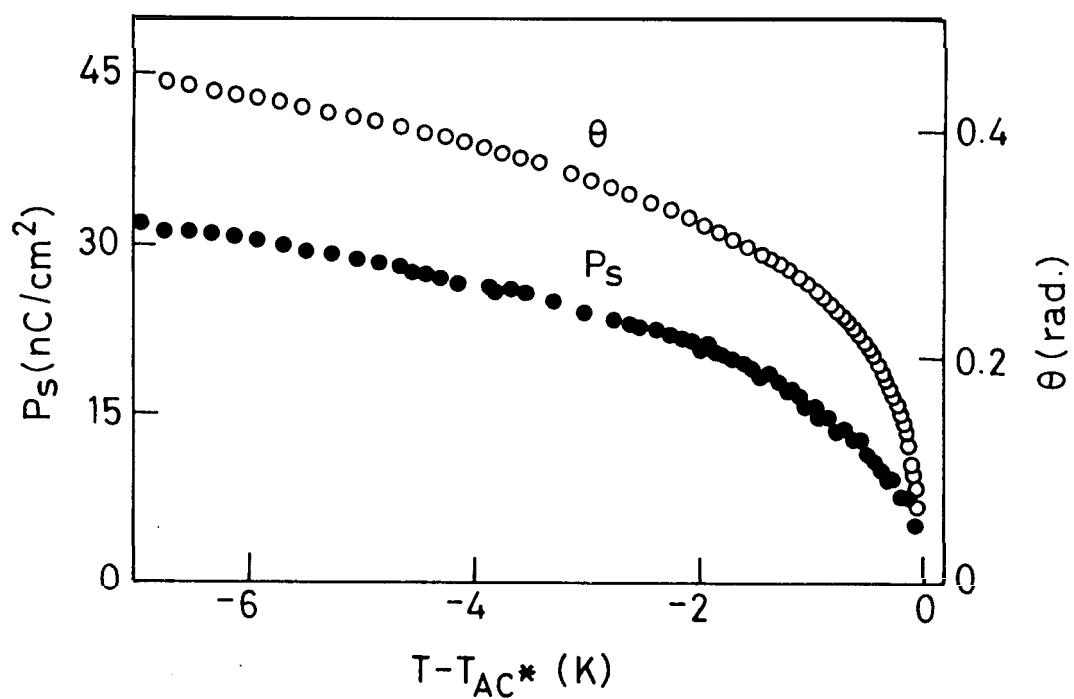


Figure 4.10: Thermal variation of P_s and θ for compound II.

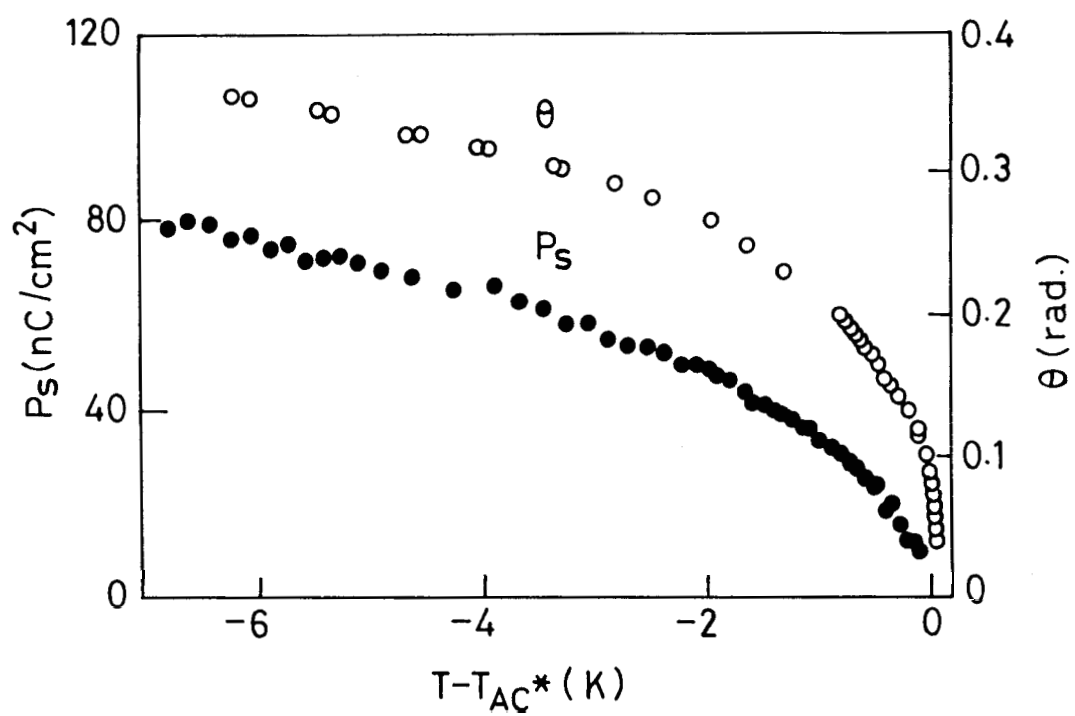


Figure 4.11: Thermal variation of P_s and θ for compound III.

(where $t = \frac{T_{AC^*} - T}{T_{AC^*}}$) describe the data well, it also showed that $\beta_1 \neq \beta_2$. Similar results have been obtained by other authors also[4].

The thermal variation of pitch p for these compounds are shown in Figures 4.12, 4.13 and 4.14. The results obtained for compound I (Figure 4.12) are in agreement with the behaviour seen earlier for this compound and its higher homolog[8]. Far below T_{AC^*} , pitch increases slowly with temperature, reaches a maximum at about 1K below T_{AC^*} and steeply drops in the range $T_{AC^*} - 0.4$ K. For compound II, the behaviour is different in the vicinity of the transition, viz., the pitch remains at the maximum value it has attained right upto the transition and does not show the precipitous drop as in compound I. In compound III pitch remains almost invariant with temperature except for a small drop in the immediate vicinity of the transition.

4.3.1 Comparison with the EMF Model

To compare our results with the predictions of the EMF model, let us recall the Equation 4.8 from section §4.1.4.

$$\tilde{P}^3 + (1 - \tilde{\theta}^2)\tilde{P} - \beta_c\tilde{\theta} = 0$$

We have used the P_S and θ data and solved the above expression numerically to obtain the values of P^* , θ^* and β_c for the three compounds. (Fitting to this equation needs P_S and θ at the same temperature. Since experimentally it was not feasible to achieve this, we fitted the θ values to Equation 4.17 and as we see from Figures 4.15-4.17 the fitting describes the data extremely well in all the cases. From the fit values we calculated the tilt angle values at the same

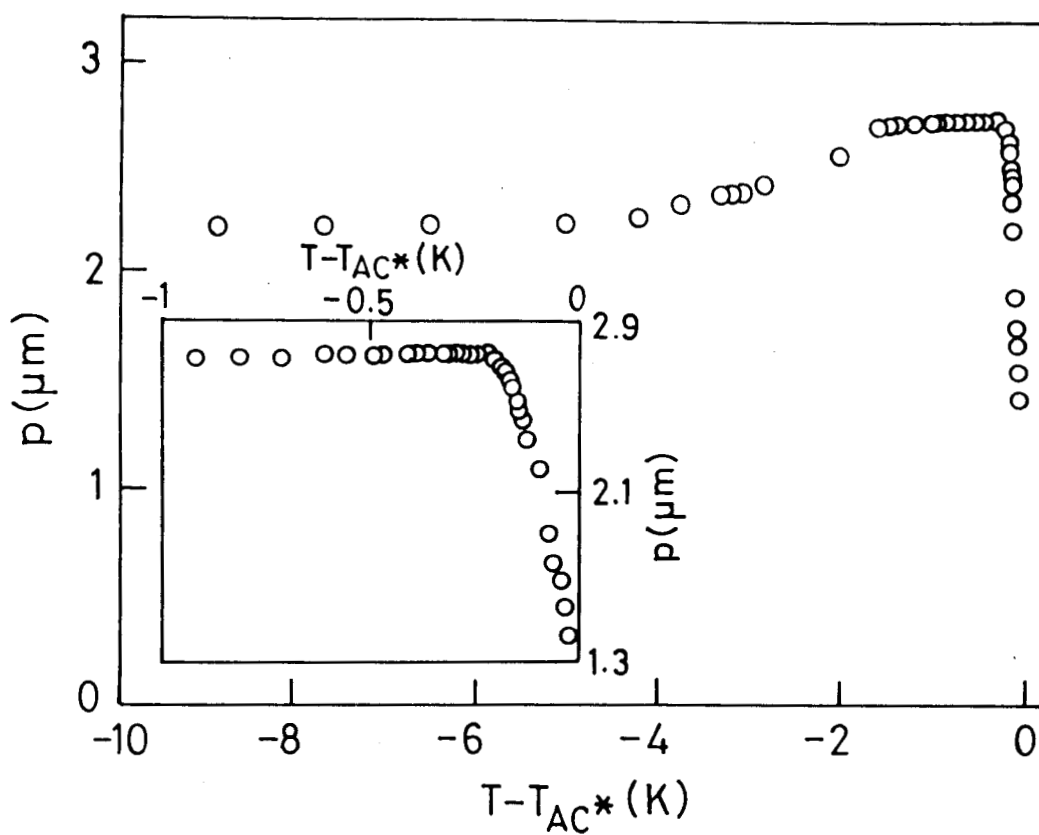


Figure 4.12: Variation of helical pitch as a function of temperature for compound I.

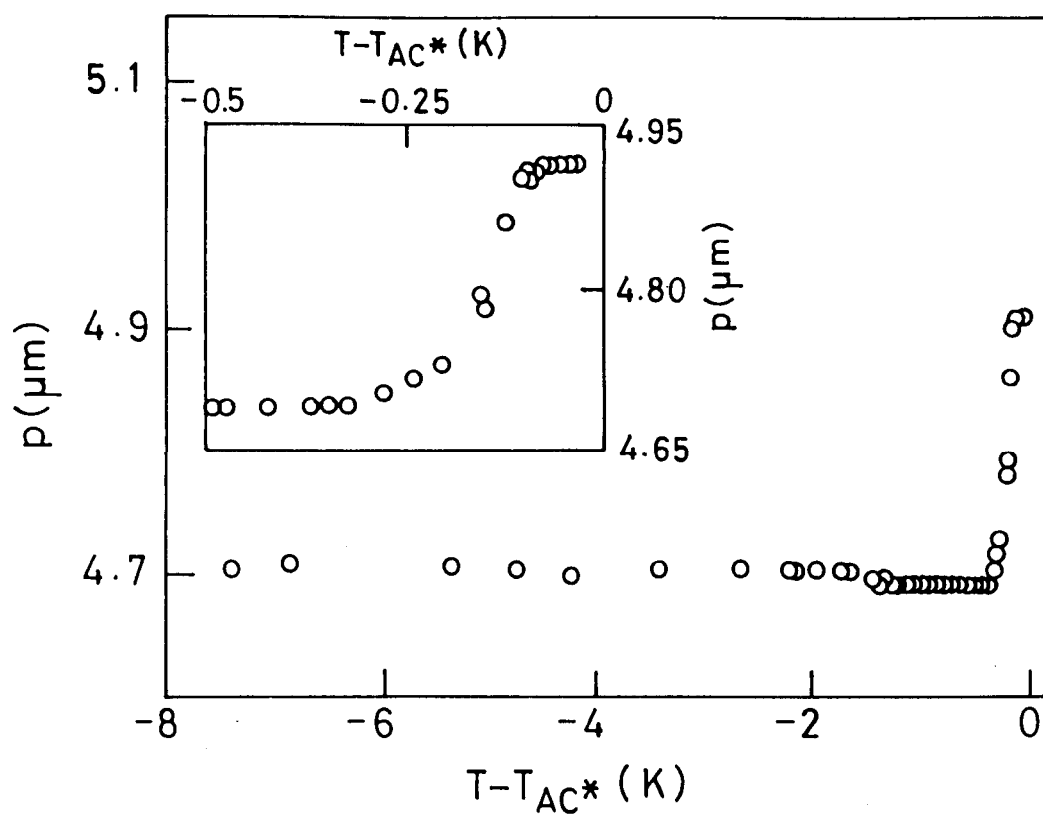


Figure 4.13: Variation of helical pitch as a function of temperature for compound II.

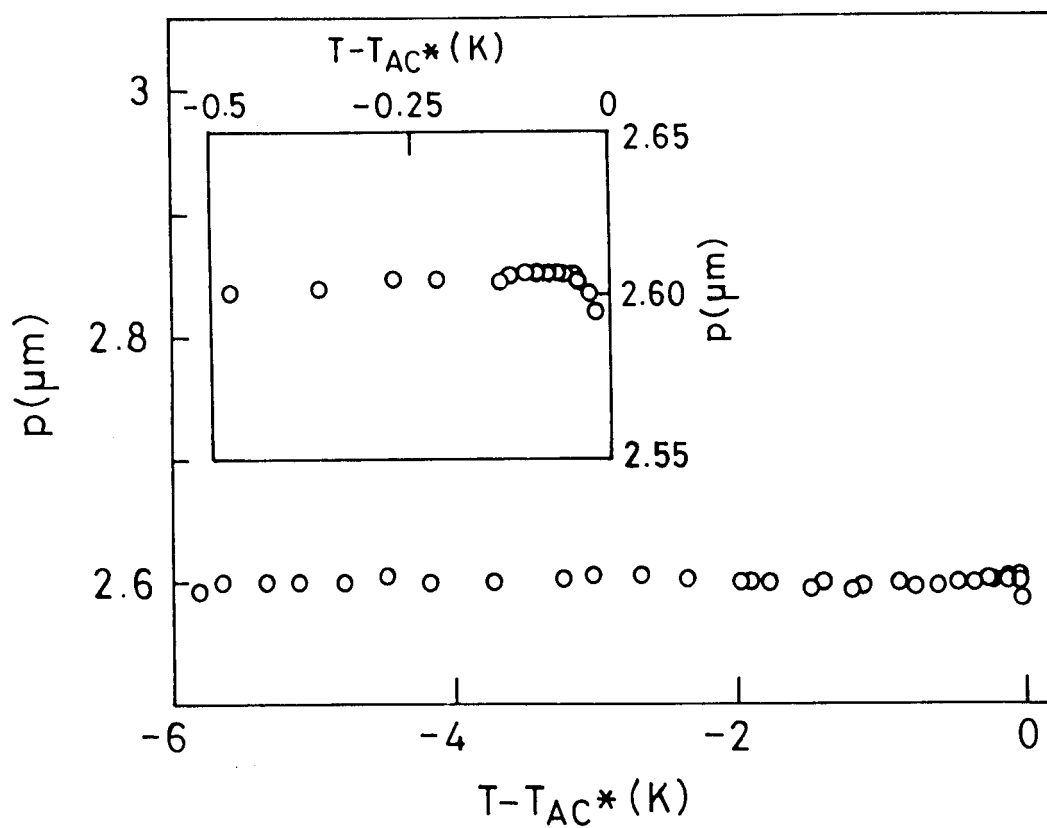


Figure 4.14: Variation of helical pitch as a function of temperature for compound III.

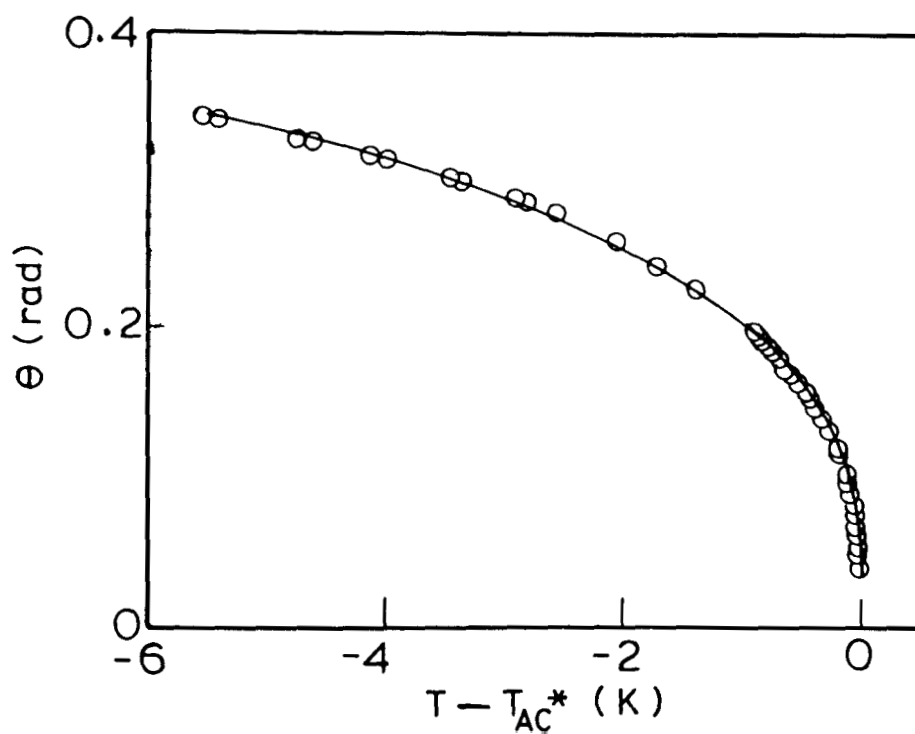


Figure 4.15: The tilt angle data fitted to a powerlaw (Equation 4.17) for compound 1. The fit represented by the solid line gives $\beta_1 = 0.296$.

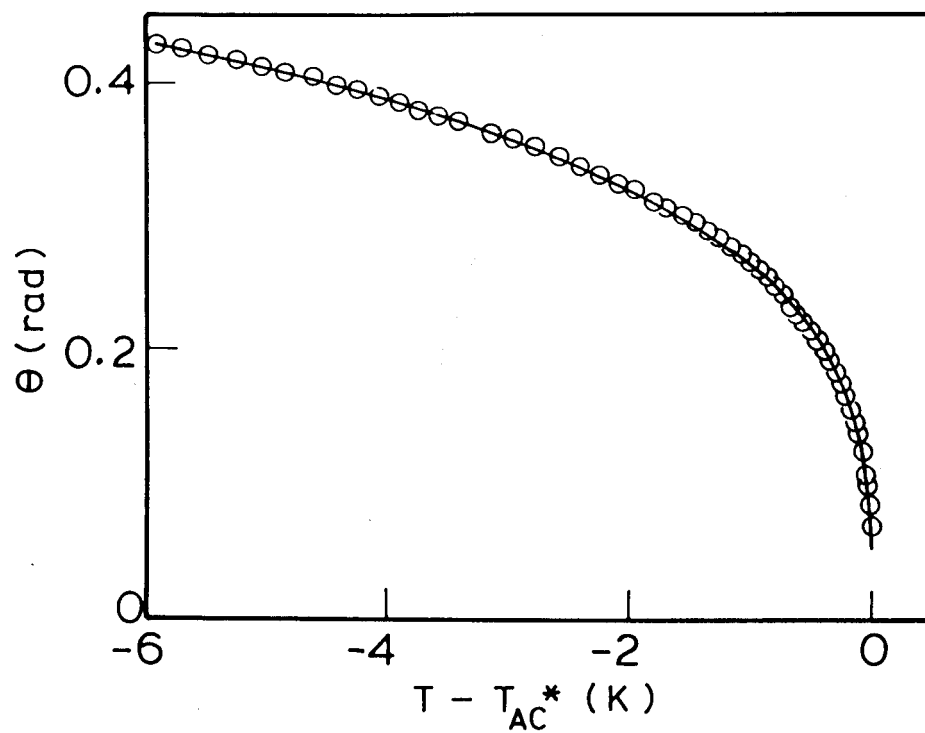


Figure 4.16: The tilt angle data fitted to a powerlaw (Equation 4.17) for compound II. The solid line representing the fit yields $\beta_1 = 0.281$.

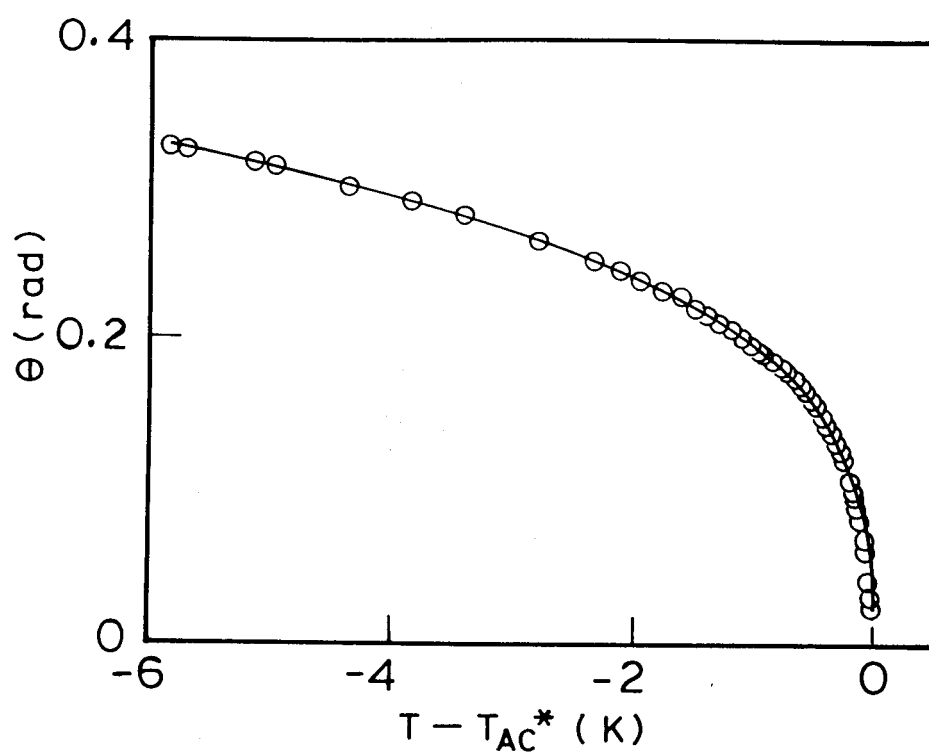


Figure 4.17: The tilt angle data fitted to a powerlaw (Equation 4.17) for compound III. The fit gives $\beta_1 = 0.336$.

temperatures as the polarisation values.) Figures 4.18-4.20 show experimental data (P_S vs θ) and the fitting (dashed line). The fit describes the data reasonably well for all the three compounds. The values of P^* , θ^* and β_c obtained are tabulated in Table 4.2. It can be mentioned here that, Pozhidayev et al[29] and Beresnev et al[30] proposed a simplified phenomenological model based on experimental data on the dynamics of the pyroelectric response. According to them, the contribution to P_S due to the spontaneous tilt of the molecules is supplemented by that resulting from the ordering of the short axes of the molecules and hence P_S is composed of terms that are linear in θ and cubic in θ , i.e.,

$$P_S = A_1\theta + A_2\theta^3 \quad (4.19)$$

Fitting done to this expression is also shown in Figures 4.18 - 4.20. The fit is represented by solid line and is observed to describe the data extremely well.

As was pointed earlier, in the framework of the generalised mean-field model, the parameter β_c determines the thermal variation of $\frac{P_S}{\theta}$ and helical pitch p . Theoretical curves for three different values of β_c are shown in Figures 4.21(a)-(c). Experimental curves of $\frac{P}{\theta}$ and pitch \tilde{p} are shown in Figures 4.22(a)-(c). The actual data of $\frac{P_S}{\theta}$ were reduced to dimensionless form by using P^* and θ^* values listed in Table 4.2. For the sake of comparison we have presented the results of compound III in Figure 4.22(b) and compound II in Figure 4.22(c).

Note that for compound I, $\frac{P}{\theta}$ does not show the 'S' shaped behaviour expected for materials with low β_c values. It may be mentioned here that an earlier high resolution study[6] on DOBAMBC also ruled out such anomalous behaviour for the $\frac{P_S}{\theta}$ ratio. In fact,, the microscopic model does not predict 'S'

Chapter 4: Polarisation-Tilt Coupling and thermal variation of Pitch...

Table 4.2: Fit parameters obtained from the EMF model

Material	P^* (nC/cm ²)	θ^* (rad)	β_c
compound I	3.7	0.38	0.29
compound II	140.7	1.2	0.49
compound III	217.5	0.5	0.32

Table 4.3: Ratio of piezoelectric bilinear to biquadratic coupling term

Material	Y at	
	$T_{AC^*} - 1K$	$T_{AC^*} - 5K$
compound I	5.35	1.55
compound II	37.3	13.9
compound III	10.7	2.7

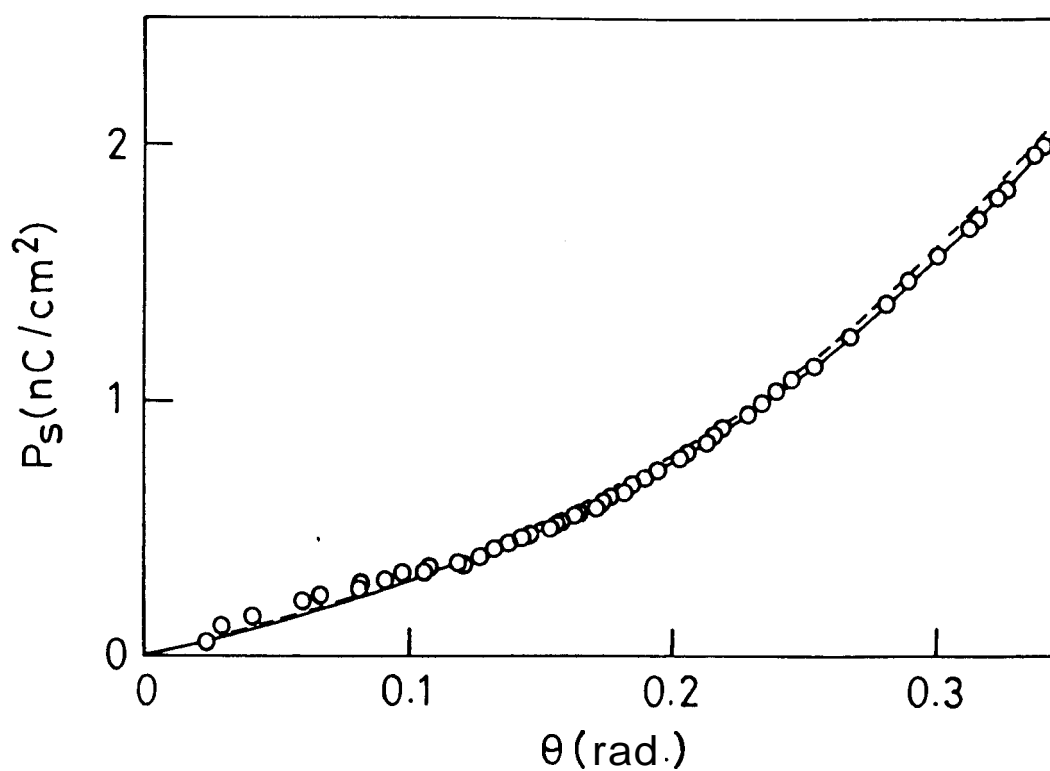


Figure 4.18: Plot of P_S vs θ for compound I. Circles denote the experimental data. Dashed and solid lines are obtained by fitting the data to Equation 4.8 and Equation 4.19 respectively.

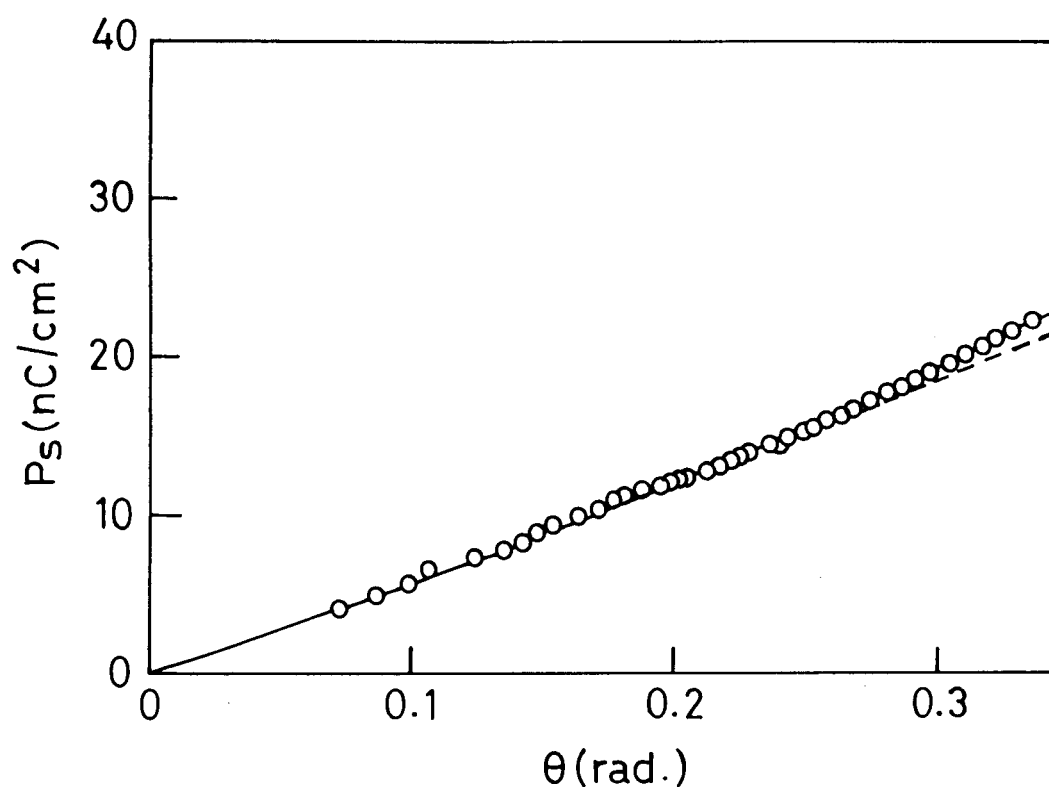


Figure 4.19: Plot of P_s vs θ for compound II. Circles denote the experimental data. Dashed line - fit to Equation 4.8. Solid line - fit to Equation 4.19. (At low θ values the dashed and the solid lines overlap completely)

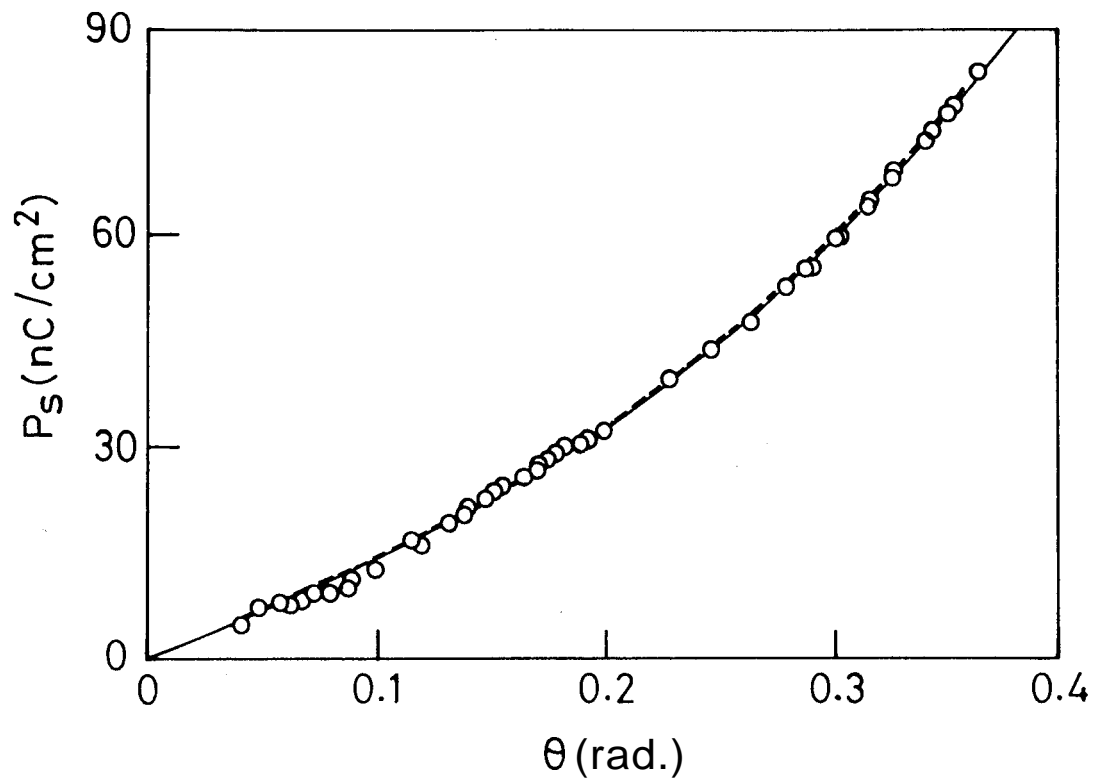


Figure 4.20: Plot of P_S vs θ for compound III. Circles denote the experimental data. Dashed and solid lines obtained by fitting the data to Equation 4.8 and Equation 4.19 respectively.

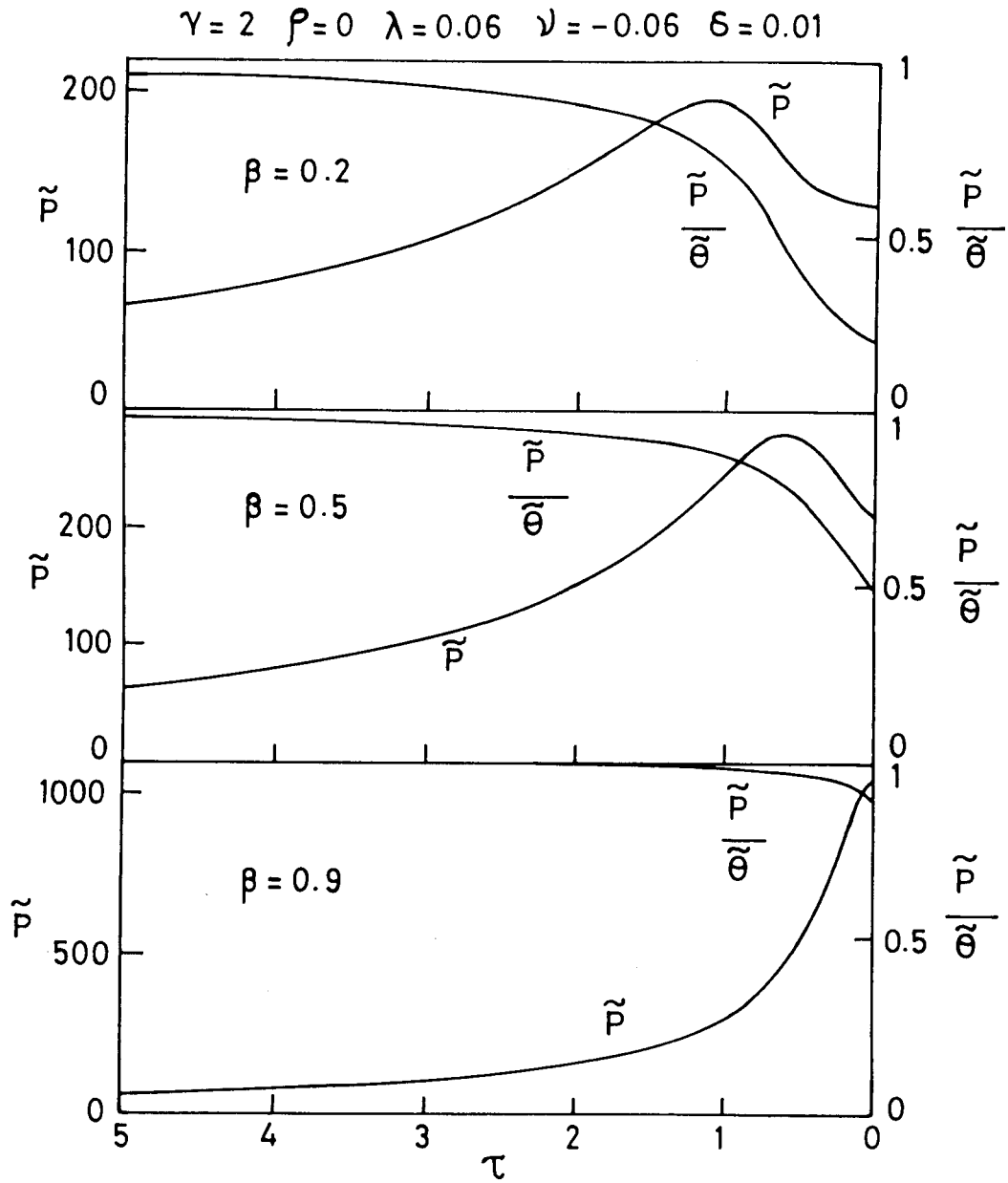


Figure 4.21: Theoretical behaviour of $\tilde{P}/\tilde{\theta}$ and \tilde{p} for different values of β_c . (from ref.[10])

Chapter 4: Polarisation-Tilt coupling and thermal variation of Pitch...

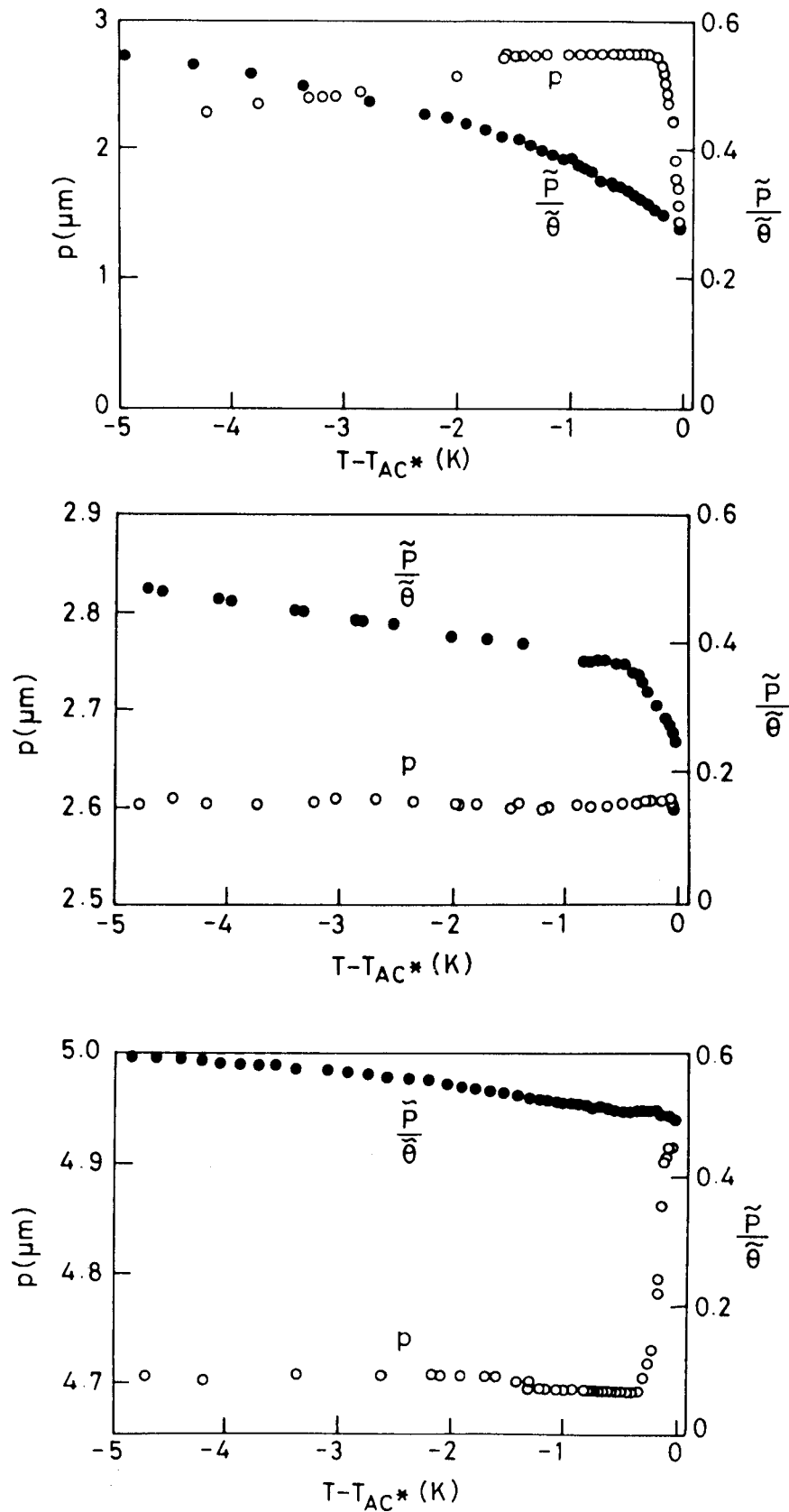


Figure 4.22: Experimental behaviour of $\tilde{P}/\tilde{\theta}$ and p for (a) compound 1 (b) compound III (c) compound II. The actual data of P_S/θ has been reduced to dimensionless form using the quantities listed in Table 4.2.

slipped variation for any value of β_c [19]. The variation of $\frac{\tilde{P}}{\theta}$ ratio and pitch p for compound II (Figure 4.22(c)) looks quite similar to the theoretical diagram (Figure 4.21(c)). $\frac{\tilde{P}}{\theta}$ is weakly dependent on temperature and p attains a maximum near the transition, but does not drop on approaching it. In the case of compound III, p remains almost invariant with temperature except for small drop in the immediate vicinity of the transition.

Although the β_c values in the theoretical and experimental cases are different the results clearly demonstrate the qualitative relationship between the values of β_c and the thermal variation of $\frac{P_S}{\theta}$ and pitch.

If, only the bilinear coupling were to be the determining factor, the behaviour seen in compound with higher P_S should have been closer to a classical case ($\frac{P_S}{\theta} = \text{constant}$). But our results for compounds II and III (P_S for III is higher than for II) show that other coupling terms are also important.

Using Equation 4.6 we have calculated the relative influence of the piezoelectric bilinear and biquadratic terms,

$$Y = \frac{2\beta_c}{\tilde{P}\tilde{\theta}} \quad (4.20)$$

Listed in Table 4.3 are the values of Y evaluated at $T_{AC^*} - 1$ K and $T_{AC^*} - 5$ K for the three compounds. It is seen that,

1. The nature of coupling is dependent on the proximity to the transition i.e., the influence of the biquadratic term is small near T_{AC^*} and large far away from it,.
2. Near the transition as well as far away from it Y (compound II) $>$ Y (com-

pound III) > Y (compound I). The latter relation is quite significant and justifies our analysis of Figures 4.22(b) and (c).

4.3.2 Comparison with the microscopic model

We recall the Equation 4.14 obtained from the microscopic model[19],

$$P_S = A_1 \theta \left[\frac{A_2 T + A_3 \theta^2}{T^2 + A_2^2 \theta^2} \right]$$

where $A_1 = \rho\mu$, $A_2 = \frac{a_1}{2K}$ and $A_3 = \frac{a_1 a_2}{4K^2}$.

We have fitted the P_S data to the above equation using a non-linear least square fit program based on the marquardt algorithm by floating the parameters A_1, A_2 and A_3 . Figures 4.23-4.25 are the plots of P_S vs. $(T - T_{AC^*})$ for the three compounds. The solid lines are the fit to Equation 4.14. It is seen from the plots that in all the cases the fitting is quite good. Using the values of A_1, A_2 and A_3 , we have calculated the dipolar term a_1 and the quadrupolar term a_2 . The values of A_1, A_2, A_3, a_1, a_2 and the ratio a_1/a_2 for the three compounds are listed in Table 4.4.

According to the theory, close to the transition a_1 dominates the potential, while away from it, the quadrupolar term a_2 takes over. From the Table 4.4 it is clear that $a_1 < a_2$ for all the compounds. One more interesting point to note here is that the ratio a_1/a_2 is highest for compound II and lowest for compound I. This again gives a strong evidence to say that the compound II is more towards the classical case even though the compound III exhibits a higher P_S value.

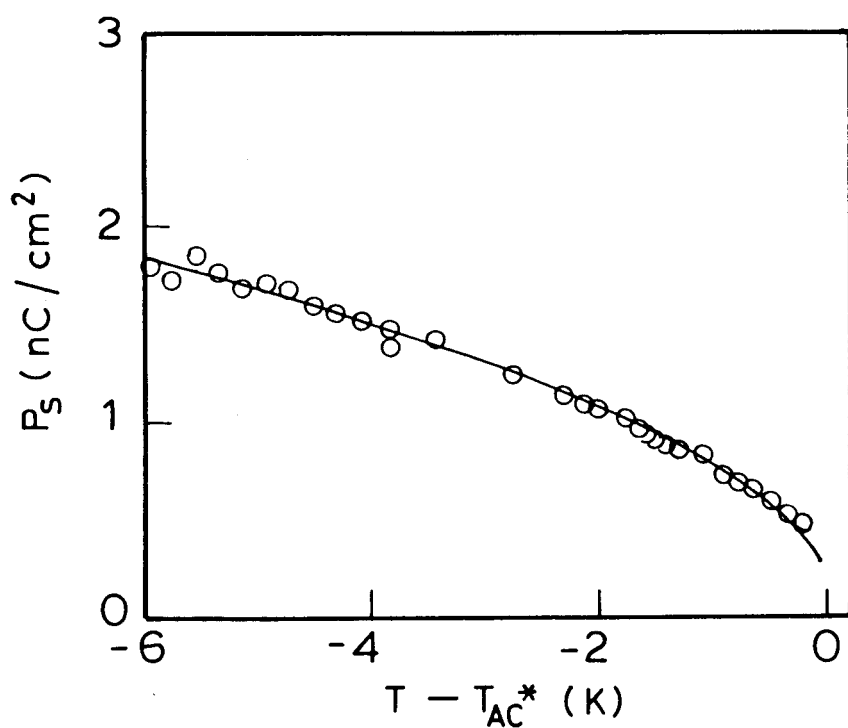


Figure 4.23: Temperature variation of P_S , for compound I, fitted to Equation 4.14 derived from the microscopic model. The solid line is the fit to the data.

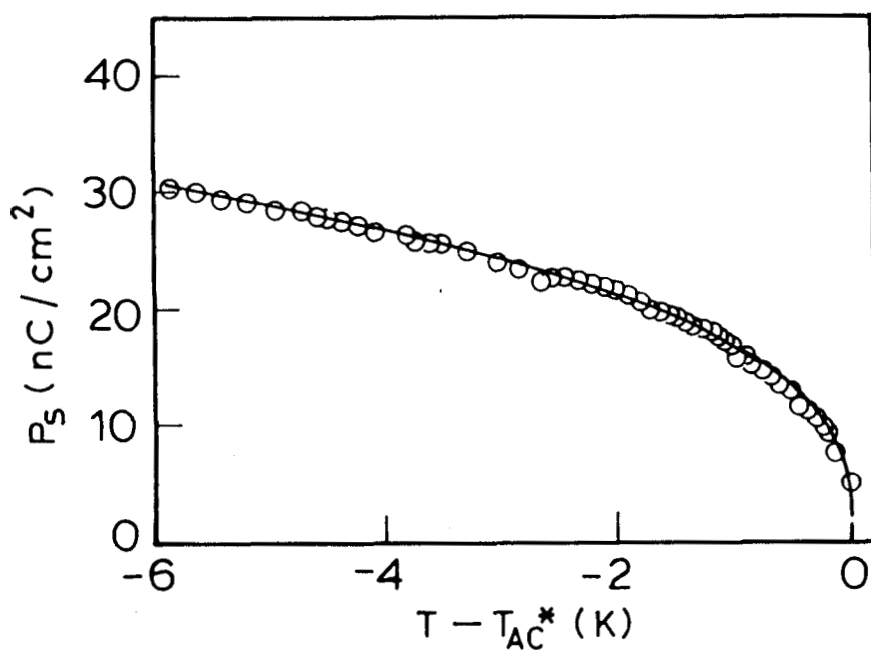


Figure 4.14: Temperature variation of P_S , for compound II, fitted to Equation 4.14 derived from the microscopic model. The solid line is the fit to the data.

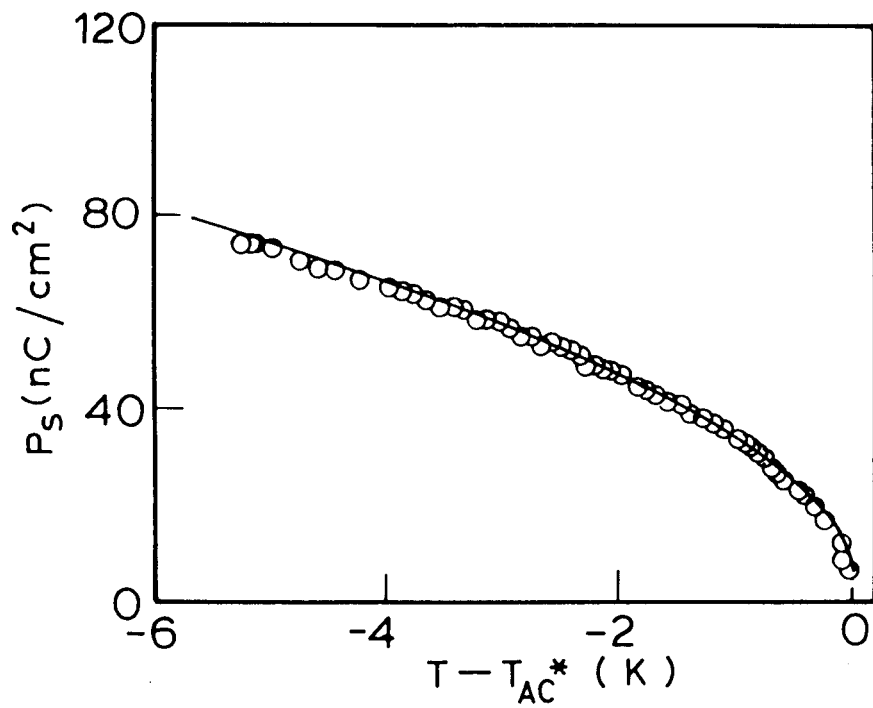


Figure 4.25: Temperature variation of P_S for compound III fitted to Equation 4.14 derived from the microscopic model. The solid line is the fit to the data.

Chapter 4: Polarisation-Tilt Coupling and thermal variation of Pitch.

Table 4.4: Fit parameters obtained from the microscopic model

Material	A_1 $(\frac{nC}{cm^2})$	A_2 (J/K)	A_3 $(J^2/\text{Å}^2)$	a_1 (J)	a_2 (J)	$\frac{a_1}{a_2}$
bound I	24.4	48.6	118.2×10^3	1.27×10^{-21}	6.37×10^{-20}	0.02
bound II	82.1	238.7	158.9×10^3	6.25×10^{-21}	1.74×10^{-20}	0.36
bound III	171.8	365.6	119.3×10^4	9.57×10^{-21}	8.55×10^{-20}	0.11

Thus the analysis based on both the generalised mean-field model and the microscopic model give the same interpretation to our data.

The coupling coefficients C and β_c of the **EMF** model can also be determined using parameters of the microscopic model[19].

$$C = \frac{a_1}{\mu} \tag{4.21}$$

We have,
$$A_1 = \rho\mu \text{ or } \mu = \frac{A_1}{\rho}$$

Substituting this in Equation 4.21 we get,

$$C = \frac{\rho a_1}{A_1} \tag{4.22}$$

Since ρ , the number density is not expected to vary drastically between these compounds, it can be treated as a constant and therefore we can write

$$\tilde{C} = \frac{C}{\rho} = \frac{a_1}{A_1} \tag{4.23}$$

The \tilde{C} values thus calculated are listed in the Table 4.5. It is seen that \tilde{C} is highest for compound II indicating that the $P_S - \theta$ coupling for this compound is closer to a classical case.

Also, expressing β_c in terms of the parameters of the microscopic model,

$$\beta_c = \frac{a_1}{2(a_2 kT)^{1/2}} \tag{4.24}$$

In the Landau model β_c is given by the dimensionless quantity $\frac{\tilde{P}}{\tilde{\theta}}$ as $T \rightarrow T_{AC^*}$. Therefore for the calculation of β_c we put $T=T_{AC^*}$. The calculated values of β_c are tabulated in Table 4.6 along with the β_c values obtained using the extended

Chapter 4: Polarisation-*Tilt* Coupling and *thermal* variation of Pitch...

Table 4.5: The bilinear coupling term calculated from the microscopic model

Material	$\tilde{C}(Vcm^2)$
compound I	5.22×10^{-23}
compound II	7.62×10^{-23}
compound III	5.57×10^{-23}

Table 4.6: The effective coupling coefficient β_c calculated from the EMF model and the Microscopic model

Material	β_c (from the EMF model)	β_c (from the microscopic model)
compound I	0.29	0.036
compound II	0.49	0.35
compound III	0.32	0.24

Table 4.7: Experimental and calculated (from the microscopic model) $\frac{P_S}{\theta}$ values as $T \rightarrow T_{AC^*}$.

Material	$\frac{P_S}{\theta}$ (exptl) (nC cm ⁻² rad ⁻¹)	$\frac{P_S}{\theta}$ (cal) (nC cm ⁻² rad ⁻¹)
compound I	2.8	3.22
compound II	58.1	57.54
compound III	145.4	175.4

EMF model. It is seen from the Table that the values obtained from the two models somewhat agree for compound II and III, but differ appreciably for compound I. The disagreement in β_c value from the two models was seen in the case of DOBAMBC (the higher homologue of compound I) also[19]. For DOBAMBC $\beta_c = 0.17$ from the extended mean-field model and 0.04 from the microscopic model.

From Equation 4.14 it is seen that when θ is very small, i.e., when $T \rightarrow T_{AC^*}$, θ^2 terms can be neglected and hence,

$$\frac{P_S}{\theta}(cal) = \frac{A_1 A_2}{T_{AC^*}} \quad (4.25)$$

The calculated $\frac{P_S}{\theta}$ ratio for the three compounds are listed in the Table 4.7 along with the experimental values. The agreement between the two values is reasonably good for all the three compounds.

In conclusion, we have studied the temperature variation of polarisation, tilt and pitch in the C^* phase of three different compounds exhibiting low, moderate and high P_S values. The results clearly show the effect of the parameter β_c on the behaviour of $\frac{P_S}{\theta}$ and pitch p . The data also demonstrate the influence of the two P_S - θ coupling terms (piezoelectric bilinear and biquadratic) on the measured parameters. All these observations are generally in good agreement with the theoretical predictions of the extended mean-field model as well as the microscopic model.

References

- [1] R. B. Meyer, L. Liebert, L. Strzelecki and P. Keller, *J. Physique Lett.* **36**, L-69 (1975).
- [2] R. B. Meyer, *Mol. Cryst. Liq. Cryst.* **40**, 33 (1977).
- [3] S. A. Pikin and V. L. Indenbom, *Sov. Phys. Usp.* **21**, 487 (1978); R. Blinc and B. Zeks, *Phys. Rev. A* **18**, 740 (1978).
- [4] B. I. Ostrovskii, A. Z. Rabinovich, A. S. Sonin, B. A. Strukov and S. A. Taraskin, *Ferroelectrics* **20**, 189 (1978).
- [5] C. Filipic, A. Levstik, I. Levstik, R. Blinc, B. Zeks, M. Glogarova and T. Carlsson, *Ferroelectrics*, **73**, 295 (1987).
- [6] S. Dumrongrattana and C. C. Huang, *Phys. Rev. Lett.* **56**, 464 (1986).
- [7] R. Blinc, B. Zeks, I. Musevic and A. Levstik, *Mol. Cryst. Liq. Cryst.* **114**, 189 (1984).
- [8] I. Musevic, B. Zeks, R. Blinc, L. Jansen, A. Seppen and P. Wyder, *Ferroelectrics* **58**, 71 (1984).
- [9] B. Zeks, *Mol. Cryst. Liq. Cryst.* **114**, 259(1984); T. Carlsson, B. Zeks, A. Levstik, C. Filipic, I. Levstik and R. Blinc, *Phys. Rev. A*, **36**, 1484 (1987).
- [10] T. Carlsson, B. Zeks, C. Filipic, A. Levstik and R. Blinc, *Mol. Cryst. Liq. Cryst.* **163**, 11 (1988).
- [11] C. C. Huang and J. M. Viner, *Phys. Rev. A* **25**, 3385 (1982).

- [12] T. Carlsson and I. Dalil, *Mol. Cryst. Liq. Cryst.* 95, 373 (1983).
- [13] R. Eidenschink, T. Geelhaar, G. Andersson, A. Dahlgren, IC. Flatiscliler, F. Gouda, S. T. Lagerwall and K. Skarp, *Ferroelectrics* 84, 167 (1988).
- [14] B. Otterholm, C. Alstermark, K. Flatiscliler, A. Dahlgren, S. T. Lagerwall and K. Skarp, *Mol. Cryst. Liq. Cryst.* 146, 189 (1987).
- [15] C. C. Huang, S. Dumrograttana, G. Nounesis, J. J. Stofko Jr. and P. A. Arimilli, *Phys. Rev. A* 35, 1460 (1987).
- [16] B. Zeks, T. Carlssoi, C. Filipic and B. Urbaiic, *Ferroelectrics* 84, 3 (1988).
- [17] B. Urbanc and B. Zeks, *Liquid Crystals* 5, 1075 (1989).
- [18] P. Pieranski, E. Guyou and P. Keller, *J. Phys.* 36, 1005 (1975).
- [19] N. A. Clark and S. T. Lagerwall, *Appl. Phys. Lett.* 36, 899 (1980).
- [20] A. Buka, K. Siemensmeyer and H. Stegemeyer, *Liquid Crystals* 6, 701 (1989).
- [21] OOBAMBC was kindly given to us by Dr. V. Surendranath.
- [22] B. Shivkumar, B. K. Sadashiva, S. K. Prasad and S. M. Khened, *Ferroelectrics*, 114, 273 (1991).
- [23] H. Diamant, I.(. Drenck and R. Pepinsky, *Rev. Sci. Instrum.* 28, 30 (1957).
- [24] S. M. Khened *Experimental studies of physical properties of ferroelectric liquid crystals*, Ph.D. thesis, (submitted to Bangalore University).

- [25] E. Sackmann, S. Meiboom, L. C. Snyder, A. E. Meixner and E. Dietz, *J. Am. Chem. Soc.* **90**, 3567 (1968).
- [26] K. Kondo, H. Takezoe, A. Fukuda and E. Kuze, *Jap. J. Appl. Phys* 21, 224 (1982).
- [27] CE8 was kindly provided to us by BDH, Poole.
- [28] I. Drevensek, I. Musevic and M. Copic, *Phys. Rev. A* 41, 923 (1990).
- [29] E. P. Pozhidaev, L. A. Beresnev, L. M. Blinov and S. A. Pikin, *JETP Lett.* **37**, 88 (1983).
- [30] L. A. Beresnev, E. P. Pozhidayev and L. M. Blinov, *Ferroelectrics* 59, 1 (1984).